



**AIAA 2003-1961**

**Contributions of the NASA Langley  
Research Center to the DARPA/AFRL/NASA/  
Northrop Grumman Smart Wing Program**

Jennifer P. Florance, Alpheus W. Burner, Gary A. Fleming,  
Craig A. Hunter, and Sharon S. Graves  
NASA Langley Research Center  
Hampton, VA 23681

Christopher A. Martin  
Northrop Grumman Corporation  
El Segundo, CA 90245

**AIAA Dynamics Specialists Conference**  
April 9-10, 2003  
Norfolk, VA

# CONTRIBUTIONS OF THE NASA LANGLEY RESEARCH CENTER TO THE DARPA/AFRL/NASA/NORTHROP GRUMMAN SMART WING PROGRAM

Jennifer P. Florance\*, Alpheus W. Burner†, Gary A. Fleming‡, Craig A. Hunter§, Sharon S. Graves¶  
NASA Langley Research Center  
Hampton, VA 23681

Christopher A. Martin#  
Northrop Grumman Corporation  
El Segundo, CA 90245

## ABSTRACT

An overview of the contributions of the NASA Langley Research Center (LaRC) to the DARPA/AFRL/NASA/Northrop Grumman Corporation (NGC) Smart Wing program is presented. The overall objective of the Smart Wing program was to develop *smart*\*\* technologies and demonstrate near-flight-scale actuation systems to improve the aerodynamic performance of military aircraft. NASA LaRC's roles were to provide technical guidance, wind-tunnel testing time and support, and Computational Fluid Dynamics (CFD) analyses. The program was divided into two phases, with each phase having two wind-tunnel entries in the Langley Transonic Dynamics Tunnel (TDT). This paper focuses on the fourth and final wind-tunnel test: Phase 2, Test 2. During this test, a model based on the NGC Unmanned Combat Air Vehicle (UCAV) concept was tested at Mach numbers up to 0.8 and dynamic pressures up to 150 psf to determine the aerodynamic performance benefits that could be achieved using hingeless, smoothly-contoured control surfaces actuated with *smart* materials technologies. The UCAV-based model was a 30% geometric scale, full-span, sting-mounted model with the *smart* control surfaces on the starboard wing and conventional, hinged control surfaces on the port wing. Two LaRC-developed instrumentation systems were used during the test to externally measure the shapes of the *smart* control surface and quantify the effects of aerodynamic loading on the deflections: Videogrammetric Model Deformation (VMD) and Projection Moiré Interferometry (PMI). VMD is an optical technique that uses single-camera photogrammetric tracking of discrete targets to determine deflections at specific points. PMI provides spatially continuous measurements of model deformation by computationally analyzing images of a grid projected onto the model surface. Both the VMD and PMI measurements served well to validate the use of on-board (internal) rotary potentiometers to measure the *smart* control surface deflection angles. Prior to the final entry, NASA LaRC also performed three-dimensional unstructured Navier Stokes CFD analyses in an attempt to predict the potential aerodynamic impact of the *smart* control surface on overall model forces and moments. Eight different control surface shapes were selected for study at Mach = 0.6, Reynolds number =  $3.25 \times 10^6$ , and + 2°, 3°, 8°, and 10° model angles-of-attack. For the baseline, undeflected control surface geometry, the CFD predictions and wind-tunnel results matched well. The agreement was not as good for the more complex aero-loaded control surface shapes, though, because of the inability to accurately predict those shapes. Despite these results, the NASA CFD study served as an important step in studying advanced control effectors.

## INTRODUCTION

Since the Wright brothers' first successful flight, aircraft designers have searched for ways to improve both the efficiency and performance of aircraft.

---

\* Aerospace Engineer.

† Senior Research Scientist. Associate Fellow, AIAA.

‡ Electronics Engineer.

§ Aerospace Engineer.

¶ Aerospace Engineer. Member, AIAA.

# Engineer Specialist. Senior Member, AIAA.

\*\* *Smart* is an industry-accepted term, but it does not imply intelligence.

This material is declared a work of the U.S.

Government and is not subject to copyright protection in the United States.

Typically, aircraft wings are designed to be most efficient at a single flight condition but suffer performance penalties at other flight conditions. These penalties may be reduced through the judicious deflection of "conventional" leading- and trailing-edge hinged control surfaces. These control surfaces affect changes in the flow field by directly varying the camber in certain regions of the wing, thereby causing changes in the aerodynamic forces and moments acting on the entire wing.

Since the 1980's, many researchers have investigated the use of fully-integrated adaptive material actuator systems (so called *smart* technologies) for performance-enhancing shape control because these devices offer a significant advantage over their conventional

counterparts: no flow-disturbing hinge lines. The DARPA/AFRL/NASA/Northrop Grumman Smart Wing program was one such effort addressing the development and demonstration of *smart* technologies.

The overall objective of the Smart Wing program was to develop *smart* technologies and demonstrate novel actuation systems to improve the aerodynamic and aeroelastic performance of military aircraft. The program began in January 1995 and was led by the Northrop Grumman Corporation (NGC) under a Defense Advanced Research Projects Agency (DARPA)-funded contract, which was monitored by the Air Force Research Laboratories (AFRL), and included partnering with NASA Langley Research Center (NASA LaRC) for technical guidance, wind-tunnel testing time and support, and CFD analyses. The program was conducted in two phases, with two wind-tunnel entries per phase. In Phase 1, two 16% geometric-scale semi-span models of an advanced military aircraft wing were each tested twice in the Langley Transonic Dynamics Tunnel (TDT). One of these wings incorporated independently-controllable conventional flap and aileron control surfaces and provided baseline aerodynamic data. The second wing, shown in Figure 1, used nickel-titanium (NiTi) shape-memory-alloy (SMA) materials technology to achieve (a) hingeless, smoothly-contoured, trailing-edge flap and aileron control surfaces and (b) variable spanwise wing twist. The deflection definitions shown in Figure 2 were used to compare the performances of the conventional and *smart* control surfaces. Detailed Phase 1 results can be found in References 1 and 2.

Phase 2 of the Smart Wing program began in January 1997. Its goals included continuing the Phase 1 *smart* technology development and maturation, demonstrating the technology on a much larger, full-span model, utilizing *smart* actuation in both leading- and trailing-edge control surfaces, and demonstrating high-rate (>60 deg/sec) *smart* actuation.

The Phase 2 model, shown installed in the TDT in Figure 3, was a sting-mounted, full-span, highly-swept (55° leading edge), 30% geometric-scale model based on the NGC Unmanned Combat Air Vehicle (UCAV) concept. To reduce program costs, only one model was constructed for this phase, with hingeless, smoothly-contoured *smart* control surfaces on the starboard wing and conventional, hinged control surfaces on the port wing. The first Phase 2 test (Phase 2, Test 1) was conducted in the TDT in March 2000, again utilizing SMA actuation. For this test, the starboard wing was outfitted with both leading- and trailing-edge *smart* control surfaces, while the port wing had only conventional trailing-edge surfaces. The *smart* trailing-



Figure 1. Smart Wing Phase 1 smart model mounted in the TDT.

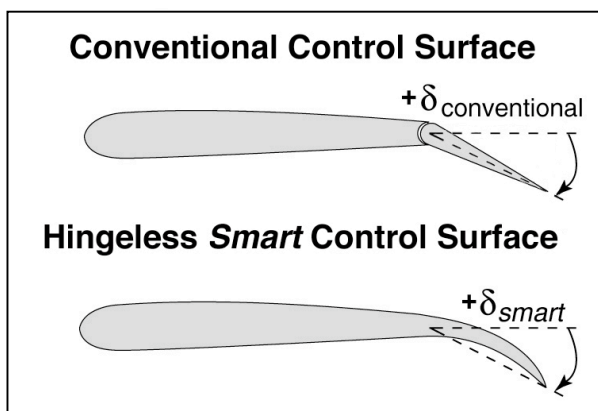


Figure 2. Deflection definitions used during the Smart Wing program.

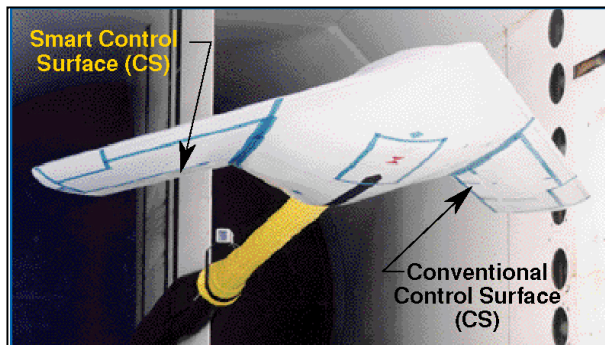


Figure 3. Smart Wing Phase 2 model mounted in the TDT.

edge control surface was comprised of six independently controlled segments that were pinned together at the trailing edge and covered with a room temperature vulcanizing (RTV) material facesheet, allowing for smoothly-contoured chordwise and spanwise shape variability. The leading-edge control surface, which is not shown in Figure 3, was a single-piece element. The focus for this entry was on the

aeroelastic effects of the *smart* leading-edge control surface and the outboard section of the *smart* trailing-edge control surface, deemed the *smart* aileron. The goal was to demonstrate that the *smart* leading edge could be used to extend roll control as the *smart* aileron became less effective with increasing dynamic pressure, a phenomenon that can lead to aileron reversal. Deflections of  $-10^\circ$  to  $+8^\circ$  for the *smart* trailing edge and  $-4.5^\circ$  for the *smart* leading edge were demonstrated, as were the anticipated aileron effectiveness trends with dynamic pressure.<sup>3</sup>

The second Phase 2 test (Phase 2, Test 2) was conducted in the TDT in April 2001. This test focused primarily on control surface deflection rate. The SMA control surfaces used previously had maximum bandwidths of less than 3Hz. To achieve the desired higher bandwidth, NGC replaced the Phase 2, Test 1 SMA-actuated six-segment trailing-edge control surface with a 10-segment control surface utilizing an alternative *smart* technology concept: eccentuator arms driven by piezoelectric ultrasonic motors. Each of the 10 segments was independently controlled, with deflections measured by 10 separate rotary potentiometers that were integrated into the actuation mechanism of each segment. All of the segments were covered with a single, unifying RTV facesheet that allowed for the generation of complex, continuously smooth, spatially-variant trailing-edge control surface shapes, as shown in Figure 4.<sup>4,5</sup> The result was a fast ( $>70$  deg/sec), morphable, hingeless control surface that maintained or improved the aerodynamic performance benefits demonstrated during the previous three tests. Uniform conventional control surface deflections of up to  $\pm 20^\circ$ , uniform *smart* control surface deflections of up to  $+20^\circ/-15^\circ$ , and 71 different *smart* control surface spanwise variation shapes were tested at Mach numbers up to 0.8 and dynamic pressures up to 150 psf.<sup>6,7,8</sup> Figures 5 and 6 show the four NGC-defined shapes that will be discussed in this paper: the baseline (no deflection), the “bathtub”, the “bird’s wing”, and a uniform deflection. The bathtub shape is defined by the deflection at the midspan of the control surface. The bird’s wing shape is defined as either a linear variation or a second-degree polynomial with inboard and outboard deflections identified.

For each of the Smart Wing tests, independent external measurements were used to aid in the verification of the control surface shapes and help quantify any aerodynamic and aeroelastic effects on the deflections of the compliant control surfaces. Two NASA LaRC-developed systems were used for this purpose: Videogrammetric Model Deformation (VMD) and Projection Moiré Interferometry (PMI). VMD is an optical instrumentation technique based on single-

camera, single-view photogrammetric tracking of retroreflective targets adhered to a model surface. The VMD technique produces highly precise deflection measurements of each discrete target location. PMI is also a video-based optical instrumentation technique for measuring model deflection. The PMI technique involves computationally analyzing images of a grid projected onto the model surface to obtain a spatially-continuous measurement of the model deformation over the entire surface within the PMI system field-of-view.



Figure 4. Photograph of the Phase 2, Test 2 *smart* trailing-edge control surface.

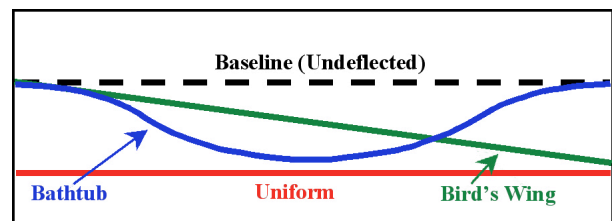


Figure 5. Four NGC-defined control surface shapes used for Phase 2, Test 2; trailing-edge profiles shown.



Figure 6. Photographs of two NGC-defined control surface shapes.

Throughout the Smart Wing program, internal sensors, such as the rotary potentiometers, were adopted as the “reference standard” for both setting the deflection angles and assessing the accuracy of the external measurements. However, because they were mounted internally, these sensors were incapable of detecting changes in the external control surface chordwise and



spanwise deflection profiles under test loading. Thus, ideally, the internal and external measurements would be considered together to provide the clearest insight into control surface behavior. This issue will be addressed further in the sections of this paper devoted to the external measurement systems.

Prior to each wind-tunnel test, Northrop Grumman personnel performed both doublet lattice and CFD analyses of the different *smart* configurations in an attempt to predict performance. To assist in this effort, NASA LaRC performed unstructured Navier Stokes CFD analyses during Phase 2 of the program. Eight different Test 2 control surface shapes were studied at Mach = 0.6, Reynolds number =  $3.25 \times 10^6$ , and + 2°, 3°, 8°, and 10° model angles-of-attack (AoAs). Results generated at the 3° AoA condition for two control surface shapes are discussed herein.

This paper highlights three of the NASA LaRC contributions to the fourth and final Smart Wing entry: VMD, PMI, and CFD analysis. A brief description of the TDT is also provided.

### **THE NASA LANGLEY TRANSONIC DYNAMICS TUNNEL (TDT)**

The four wind-tunnel tests performed for the Smart Wing program were all conducted in the NASA Langley Transonic Dynamics Tunnel (TDT). The TDT, shown in Figure 7, is a closed circuit, continuous flow, single return wind tunnel. The test section is 16-foot square with cropped corners. It is capable of testing over a range of stagnation pressures from near zero to atmospheric and Mach numbers from near zero to 1.2, using either an air or R-134a test medium. In the event of an instability, the TDT also has the capability to reduce wind speed rapidly through the activation of four bypass valves that connect the test section area to the opposite leg of the wind-tunnel circuit.<sup>9</sup> Designed specifically for aeroelastic testing, the TDT has been used for decades to conduct numerous aircraft and rotorcraft aeroelastic and aeroservoelastic tests.

### **VIDEOGRAMMETRIC MODEL DEFORMATION (VMD) MEASUREMENTS**

The videogrammetric model deformation (VMD) measurement technique is an optical method characterized by automated image processing, sub-pixel resolution, near routine, near real-time measurements, and high data volume with minimum impact to wind-tunnel test productivity.<sup>10,11</sup> The technique consists of a



*Figure 7. The NASA Langley Transonic Dynamics Tunnel (TDT).*

single-camera, single-view, photogrammetric solution from digital images of targets placed on a wing or control surface with one coordinate known. Except for the targets, the technique is non-intrusive. The VMD technique was used during all four Smart Wing entries in the TDT to obtain deformation measurements. For the first three tests, the measurements were made at three spanwise locations along the main body of the *smart* wing and at spanwise locations on the *smart* control surface. For the first full-span model entry (Phase 2, Test 1), measurements were also made on the conventional flap and aileron.<sup>12,13</sup> The final Smart Wing test highlighted here acquired VMD data at only two spanwise locations on the *smart* control surface. It was also the first facility test in which the recently developed and enhanced model deformation measurement system<sup>11</sup> was used as a primary measurement system. During the test, this enhanced VMD system was operated in an automated, full frame mode at 30 Hz and acquired over 2000 data points without a significant malfunction.

### **Setup and Calibration**

Retro-reflective tape targets were used as optical targets during all Smart Wing tests to ensure high-contrast imagery. The tape targets are 4 mils thick and have a root-mean-square (rms) surface roughness of 200  $\mu$ inches. When a light source is positioned near the camera, the light retro-reflected from the tape targets can greatly exceed that possible with white diffuse targets, resulting in high-contrast images (Figure 8) in which the targets are easily discriminated from the background. For the final Smart Wing test, the hingeless control surface consisted of ten independently controlled segments that were used to produce various control surface shapes. Ten 0.5-inch diameter retro-reflective tape targets were placed equally-spaced and

centered on the lower surface of two of those segments: segments 3 and 6, shown in Figure 9. There were five targets per segment, with one target of each segment row positioned on the main wing element side of the virtual *hingeline* (i.e., where a hingeline would have been for a conventional control surface) of the *smart* control surface to serve as a reference point. The general location of the targets is identified on the left side of Figure 10. Other targets visible on the figure were used in Phase 2, Test 1. A more detailed image of the targets on the control surface is shown in Figure 11.

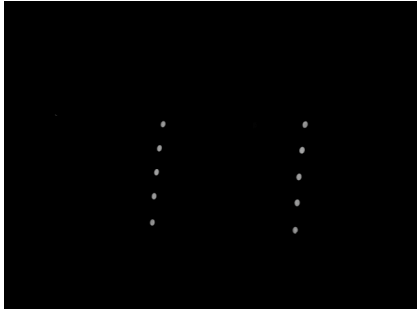


Figure 8. Unprocessed image from the VMD data camera.



Figure 9. Photograph of the Phase 2, Test 2 smart trailing-edge control surface highlighting the segments monitored by VMD.

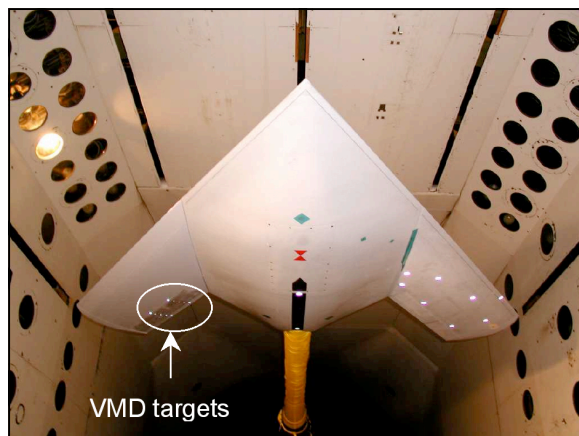


Figure 10. Photograph of the lower surface of the model showing the VMD retro-reflective tape targets on smart control surface segments 3 and 6.

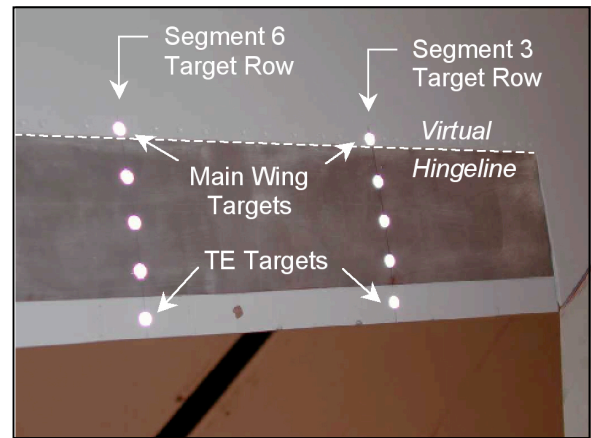


Figure 11. Close-up photograph of the retro-reflective targets on the lower side of the control surface on the smart wing.

In-tunnel calibration of the VMD system was accomplished using a calibration fixture. This fixture, which consists of an array of targets with known spatial coordinates, was initially used to determine lens distortion and principal distance, as well as to determine the orientation of the camera in the desired coordinate system. For this phase of the calibration, the fixture was placed to fill the field-of-view of the camera for the distortion computations and was not necessarily aligned to the model. Once the measurement system was set up with the proper view of the model, the calibration fixture was aligned to the control surface of the *smart* wing (Figure 12) in order to determine the pointing angles and location of the camera via photogrammetric space resection. Since the primary interest for this test was the deformation of the control surface, the Y-axis of the calibration fixture was aligned with the virtual *hingeline* of the control surface. To simplify the calibration process, this procedure was performed at only a single model pitch angle of  $1.6^\circ$ . (Note that for the remainder of this paper, both wind-off pitch angles and wind-on angles-of-attack (AoAs) will be referred to as AoAs). The X-axis of the orthogonal coordinate system was thus perpendicular to the *hingeline* at that angle. Consequently, the computed Z-coordinates for the targets were only calibrated strictly at model AoAs of  $1.6^\circ$ . At other model AoAs, the Z-coordinates would need additional corrections determined as a function of those angles.

After calibration, the VMD measurement process begins with the acquisition and digitization of a live video stream, which for the final Smart Wing test was automatically triggered by the facility Data Acquisition System (DAS) at 30 samples per second for 2 seconds as each data point was acquired. The resulting image data were then reduced using techniques discussed in

References 11 and 12. The final output was several data files containing facility DAS parameters, mean X,Y,Z target location data for each facility-triggered data point, and X,Z time histories.

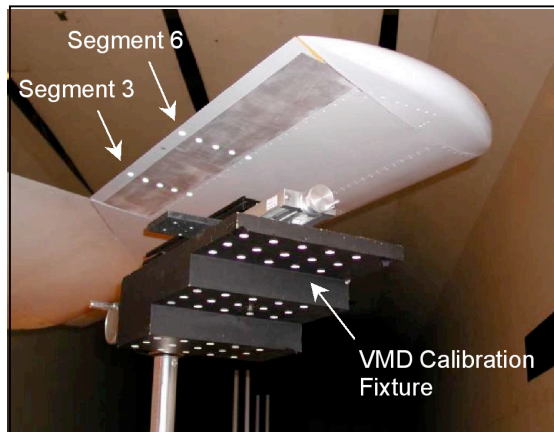


Figure 12. Photograph of the VMD calibration plate/fixture mounted underneath the smart wing.

## Results

During the test, both static and dynamic time histories of the shapes of segments 3 and 6 were automatically acquired and reduced with the enhanced videogrammetric measurement system. A typical plot of mean Z versus mean X of the control surface for five different control surface deflections acquired at Mach = 0.8,  $q = 150$  psf, and AoA =  $1.6^\circ$  is presented in Figure 13. This data represents the profiles of the lower surfaces of segments 3 and 6 of the *smart* control surface sampled at the five target locations on each. The target on the main wing element associated with each segment has an X-value of about -7.2 inches, whereas the target nearest the trailing edge of the control surface has an X-value of about -1.7 inches. The standard deviations of the 60 samples used to compute the means of Z are generally less than the symbol size and are typically around 0.01 inch. Third order least square fit line plots of the X, Z data are superimposed.

As mentioned previously, the primary objective of the VMD measurement system for the final Smart Wing test was to measure the shapes of segments 3 and 6 of the control surface. Since the surfaces are curved as they deflect, any single angle used to describe the deflection of each segment is dependent on how the angle is defined and will not truly capture the external shape. Thus, instead of angular resolution, VMD accuracy will be discussed in terms of the short-term (back-to-back repeat data points) and within-run precision of the coordinate describing the contour of the

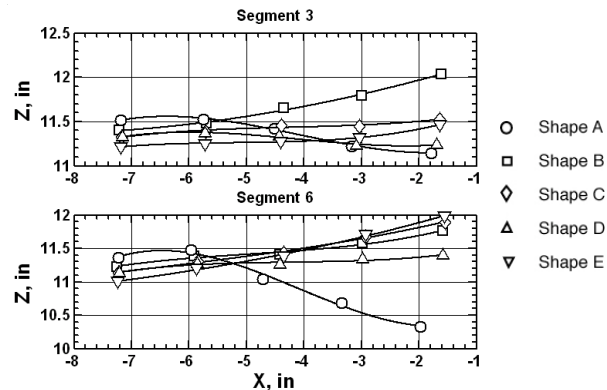


Figure 13. Typical VMD plot layout showing 5 of the 71 different control surface deflections tested; Mach = 0.8,  $q = 150$  psf, and AoA =  $1.6^\circ$ .

lower surface: Z. The difference,  $\Delta Z$ , in mean Z between two repeat data points (separated by 45 seconds and acquired at Mach = 0.6,  $q = 150$  psf, and AoA =  $-2.4^\circ$ ) is plotted versus X in Figure 14 to serve as an indicator of short-term repeatability. For these points, the short-term repeatability was generally better than 0.5 mil (0.0005 inch) with a worst-case difference of 0.6 mil. The within-run standard deviations of Z for wind-on runs without activation of the control surface segments were generally less than 12 mil with a typical value less than 10 mil. If the fluctuations of the data acquired are assumed to be random, then the standard deviation of the mean of the Z-values would be approximately equal to 10 mil divided by the square root of 60, or less than 1.3 mil for the wind-on data. The standard deviations for wind-off data runs were typically less than 4 mil, with the majority of the data having standard deviations of 2 mil or less. If the variations were random in nature, the standard deviation of the mean of Z for the wind-off runs would be less than 0.3 mil. These values indicate that (1) the standard deviation is relatively independent of AoA and (2) the standard deviations are greater wind-on than wind-off.

Wind-off bench tests performed prior to the final Smart Wing test indicated that a target placed on the main wing element near the virtual *hingeline* would remain essentially stationary during deflections of the control surface. This wind-off behavior was confirmed during the wind-tunnel entry and is demonstrated in Figure 15, where the X, Z coordinates of segments 3 and 6 are plotted for uniform control surface deflections ranging from  $-15^\circ$  to  $20^\circ$  with AoA fixed at  $-0.4^\circ$ . Analysis showed that the standard deviations for the wing element targets in this data set were 0.8 mil and 2.9 mil for segments 3 and 6, respectively. The maximum Z-displacements for those two targets were 2.4 mil and



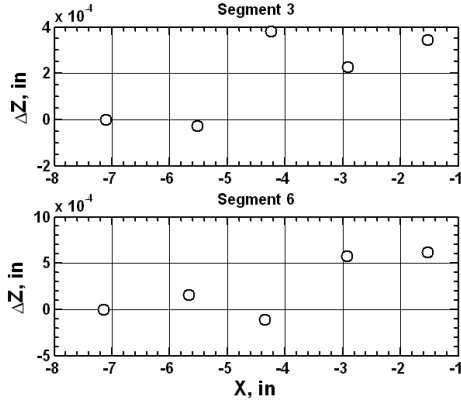


Figure 14. Difference in Z for back-to-back repeat points,  $Mach = 0.6$ ,  $q = 150$  psf,  $AoA = -2.4^\circ$ .

8.5 mil, respectively. Wind-on VMD measurements, however, did not observe the same main wing target stability. This is evident for the wind-on data previously presented in Figure 13, where the movement of the two wing targets is up to 0.4 inches. This motion was nearly 100 times greater than was seen wind-off, and analysis showed that the motion was also over 300 times the standard deviation of mean wind-on repeat data, indicating a real effect. Analysis of the VMD data for wind-on conditions also revealed that both the main wing target and the target on the control surface segment nearest the virtual *hingeline* consistently had Z-deflections of the opposite sign from the remaining three targets nearer the control surface trailing edge for both segments. An example of this behavior is evident in Figure 16, which shows the X, Z coordinates as the control surface is deflected from the NGC-defined  $11.5^\circ$  mid-bathtub shape to an approximate  $0^\circ$  uniform (undeflected) shape at  $Mach = 0.6$ ,  $q = 150$  psf, and  $AoA = 1.73^\circ$ . Wind-off, the control surface targets all demonstrated deflections of the same sign, with the wing target remaining almost stationary as previously discussed. These wind-on effects are most likely due to a combination of flow induced wing twist and local reaction of the main wing element to the control surface actuation. These aerodynamic and aeroelastic effects could not be measured with traditional onboard gages alone, such as the rotary potentiometers used during this final Smart Wing test. This illustrates the value of both independent remote optical measurements and the acquisition of extensive wind-off data. To better emphasize the lower surface profiles, the remaining VMD surface contour plots shown in this paper have been normalized by zeroing the main wing element Z-coordinate. Figure 17, for example, shows the normalized data plot corresponding to Figure 16. The change in the profiles as the surfaces are deflected is clearly evident.

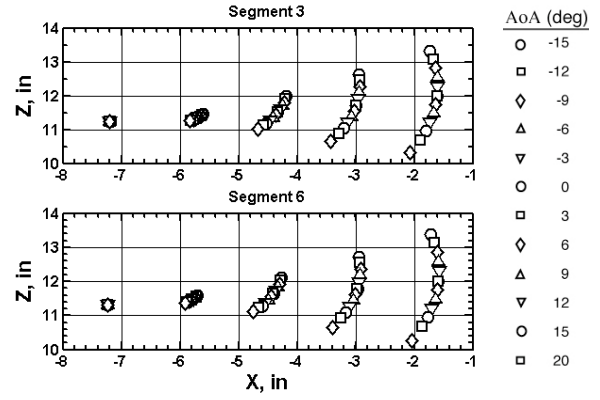


Figure 15. Coordinates as smart control surface segments were deflected uniformly from  $-15^\circ$  to  $20^\circ$ , wind-off,  $AoA = -0.4^\circ$ .

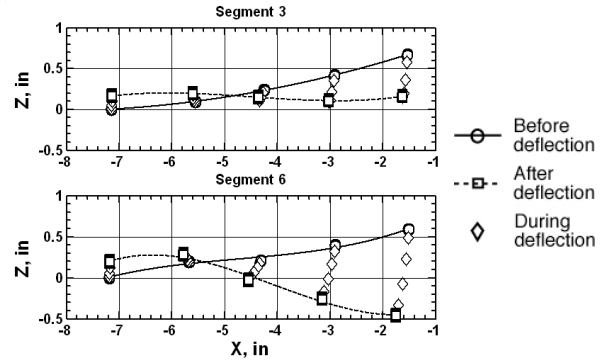


Figure 16. Data plot showing the typical movement of targets during a wind-on control surface deflection ( $11.5^\circ$  mid-bathtub shape to  $\sim 0^\circ$  uniform),  $Mach = 0.6$ ,  $q = 150$  psf,  $AoA = 1.73^\circ$ .

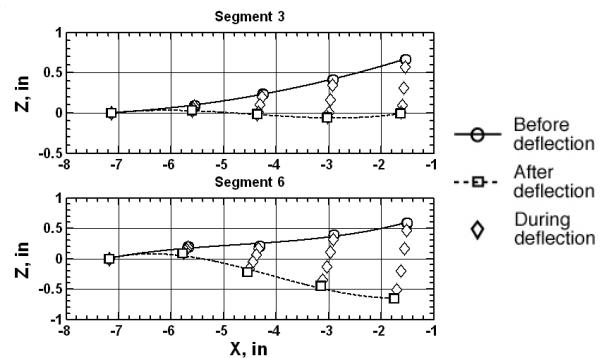


Figure 17. Data plot corresponding to Figure 16 with Z coordinates normalized by the main wing target Z values.

Figures 16 and 17 also show an example of the dynamic data acquired with the VMD system, capturing the movement of the control surface segments during a deflection. The associated time histories of the five

targets for segments 3 and 6 are presented in Figure 18. Based on the VMD data, this deflection occurred in little less than 0.13 seconds for segment 3 and 0.17 seconds for segment 6. For comparison, the deflection times as measured with the onboard potentiometers (with much better temporal resolution) were 0.10 and 0.15 seconds for segments 3 and 6, respectively.

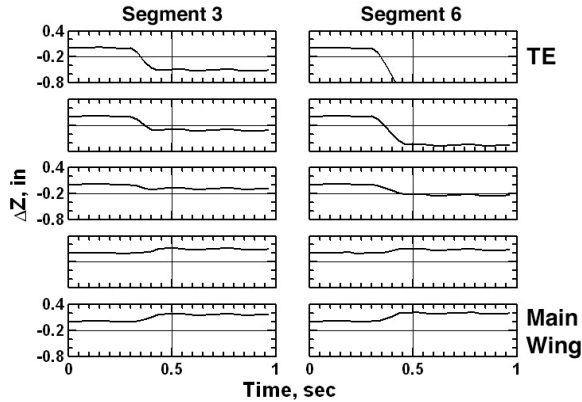


Figure 18. Time histories for segment 3 and 6 data shown in Figures 16 and 17.

The effects of changes in model AoA on the X, Z coordinates for segments 3 and 6 for four different control surface shapes are presented in Figure 19. The data is normalized and represents a  $-4.4^\circ$  to  $7.6^\circ$  AoA-polar acquired at Mach = 0.6,  $q = 150$  psf. Figure 19(a) represents the NGC-defined  $10^\circ$  bathtub shape. Figure 19(b) presents a baseline, where the control surface is undeflected. Figures 19(c) and 19(d) demonstrate data acquired for a  $10^\circ$  uniform deflection and the NGC-defined low bird's wing deflection (linear variation from  $0^\circ$  inboard to  $8.5^\circ$  outboard), respectively. For all four cases, the X, Z coordinates change considerably even though the control surface itself was not being actuated. As discussed previously, this kind of error was expected since the videogrammetric system was calibrated at only one angle-of-attack (AoA =  $1.6^\circ$ ). More accurate control surface measurements could be made if additional calibrations were performed as a function of AoA.

As previously mentioned, quantifying an angular value for the deflection of a contoured surface depends on how that angle is defined. The onboard rotary potentiometer angles for each segment were determined via a wind-off calibration using a 2-point arctangent computation in X, Z control surface centerline coordinates of the *hingeline* and the trailing edge (Figure 2). For comparison purposes, the videogrammetric angles were determined by four different methods for a wind-off control surface

deflection sweep of  $-15^\circ$  to  $20^\circ$  at AoA =  $-0.4^\circ$ , with sign chosen to make trailing-edge down positive. Two of the methods consisted of 2-point arctangent computations in X, Z coordinates using (1) the trailing-edge and main wing element targets and (2) the trailing-edge target and target nearest the *hingeline*, but still on the movable control surface. The other two methods consisted of linear least squares fits to (3) all the targets and (4) all targets except the main wing element target. The resulting videogrammetric angles are plotted against the corresponding potentiometer angles in Figure 20, with circles, squares, diamonds, and triangles representing the four methods above, respectively. Fifth-order least squares polynomial fits of each method are also included on the figure. Methods (1) and (3) yield very similar results, as do methods (2) and (4). There is a negative bias of about  $8^\circ$  for the VMD angles since they were measured from targets on the lower surface, which has a negative inclination to the control surface centerline used by the potentiometers. After accounting for this bias, methods (1) and (3) tend to underestimate the control surface segment angle by about 6% to 11% (as compared to the potentiometer data), whereas methods (2) and (4) tend to overestimate by about 13%. However, due to the high precision of the videogrammetric data, calibration based on the potentiometers at a given AoA is possible. A fifth order fit to the data yields residuals (between data and fit) with a standard deviation of  $0.11^\circ$  and  $0.08^\circ$  for segments 3 and 6, respectively. These residuals are shown in Figure 21. For a first-order fit, the residuals are approximately twice as large. In most cases, the residuals based on the four methods are within  $0.01^\circ$ , with worst-case agreement of  $0.02^\circ$ . Thus the four methods are essentially equivalent after calibration. The maximum deviations of the residuals after calibration are  $0.3^\circ$  and  $0.2^\circ$  for segments 3 and 6, respectively. Thus the videogrammetric data can be calibrated to within several tenths of a degree if a single parameter (such as segment deflection angle as defined by the potentiometers) is desired to describe the control surface deflection at each segment. The linearity and repeatability specifications of the rotary potentiometers are 0.1% and 0.01% of full scale ( $340^\circ$ ), or  $0.34^\circ$  and  $0.034^\circ$ , respectively. Thus it is expected that a large fraction of the residuals may be due to inaccuracies in the potentiometers. Since the repeatability of the videogrammetric data is on the order of several hundredths of a degree, it is possible to calibrate to those levels at specific AoAs and control surface settings. Optimum calibration using the rotary potentiometers as the reference should consist of corrections represented with a response surface as a function of both AoA and potentiometer readings.



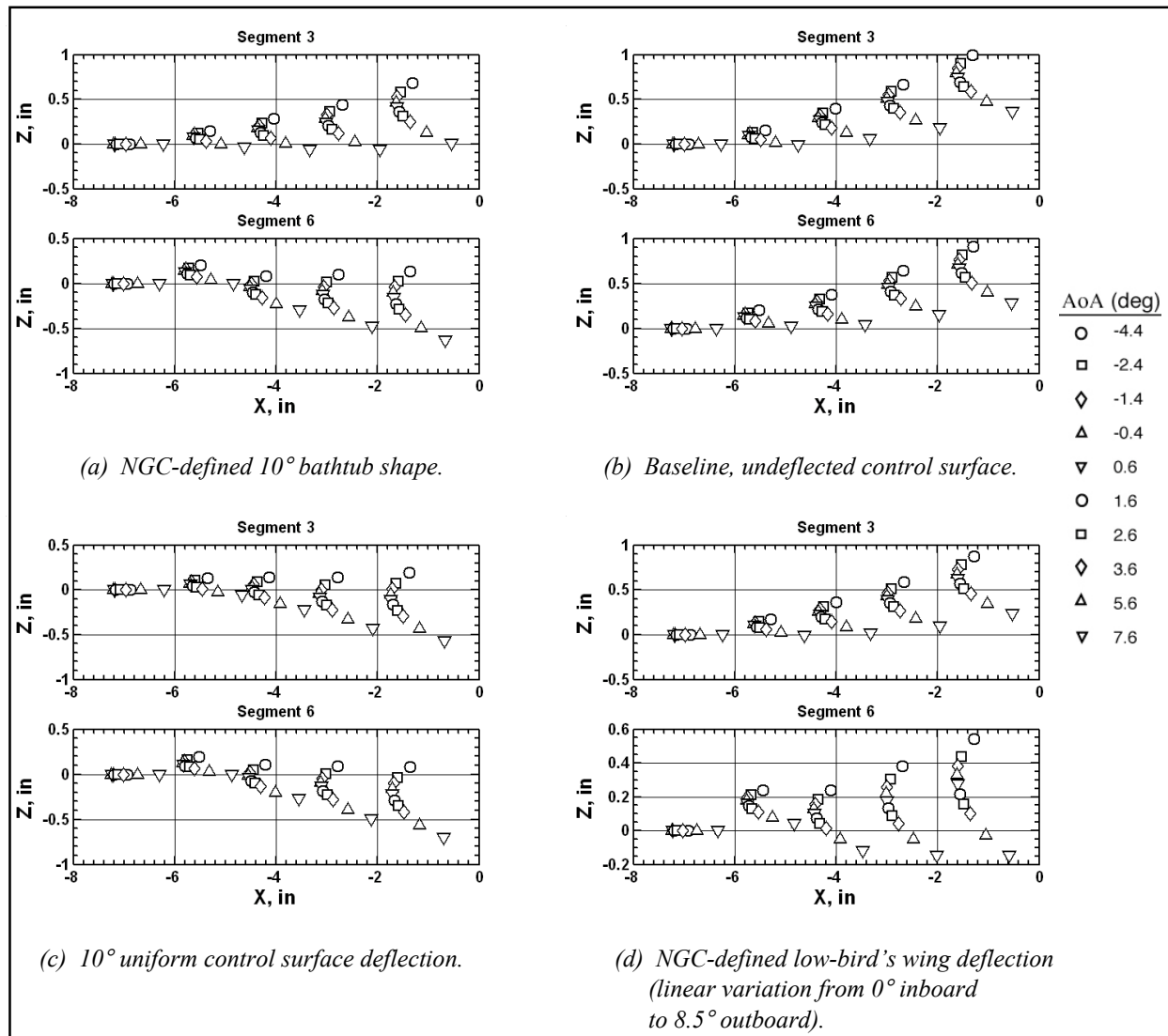


Figure 19. Effects of changes in model pitch angle on the X, Z coordinates for four different control surface shapes, Mach = 0.6,  $q = 150$  psf, AoA =  $-4.4^\circ$  to  $7.6^\circ$ .

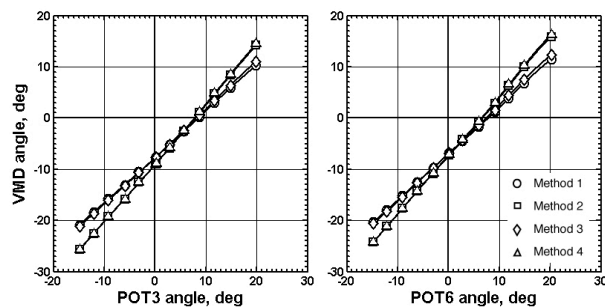


Figure 20. VMD angles versus angles from onboard potentiometers for wind-off uniform smart control surface deflections, AoA =  $-0.4^\circ$ .

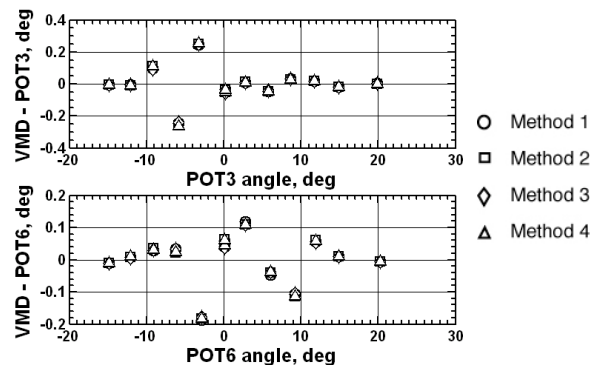


Figure 21. Residuals from fifth-order least squares polynomial fits to data in Figure 20.

## **PROJECTION MOIRÉ INTERFEROMETRY (PMI)**

A Projection Moiré Interferometry (PMI) system was used during the second Smart Wing Phase 1 entry and during both of the Phase 2 entries for optical measurement of the Smart Wing control surface deformation. The PMI technique is illustrated in Figure 22. As shown in Figure 22(a), a projection system is used to project a grid of equispaced, parallel lines onto the wind-tunnel model surface. The projector system is typically aligned such that its optical axis is perpendicular to the surface being measured. A Charge Coupled Device (CCD) camera is positioned to view the model at a 30-45° angle inclined from the projector optical axis. The projector and camera must lie within a plane perpendicular to the projected grid lines. Images of the grid lines projected onto the model are acquired in baseline (wind-off) and loaded (wind-on) conditions. An example PMI raw data image with an approximate 1.2-x 1.2-meter field-of-view is shown

in Figure 22(b). Image processing routines are then used to remove camera perspective distortion and interfere the acquired images with a computationally generated reference grid, resulting in interferograms containing moiré fringes (Figure 22(c)). These fringe patterns are further processed offline to obtain a quantitative, spatially continuous representation of the model surface shape or deformation, as shown in Figure 22(d). Reference 14 contains further details of the PMI technique as applied to measuring wind-tunnel model deformation.

### **Wind-Tunnel Installation**

Figure 23 schematically shows the PMI system hardware installation for the second Smart Wing Phase 2 test. The optical components were installed at a streamwise location closely matching the model pitch axis. The PMI system projector head was installed underneath the TDT test section floor and aligned to project a grid onto the underside of the Smart Wing

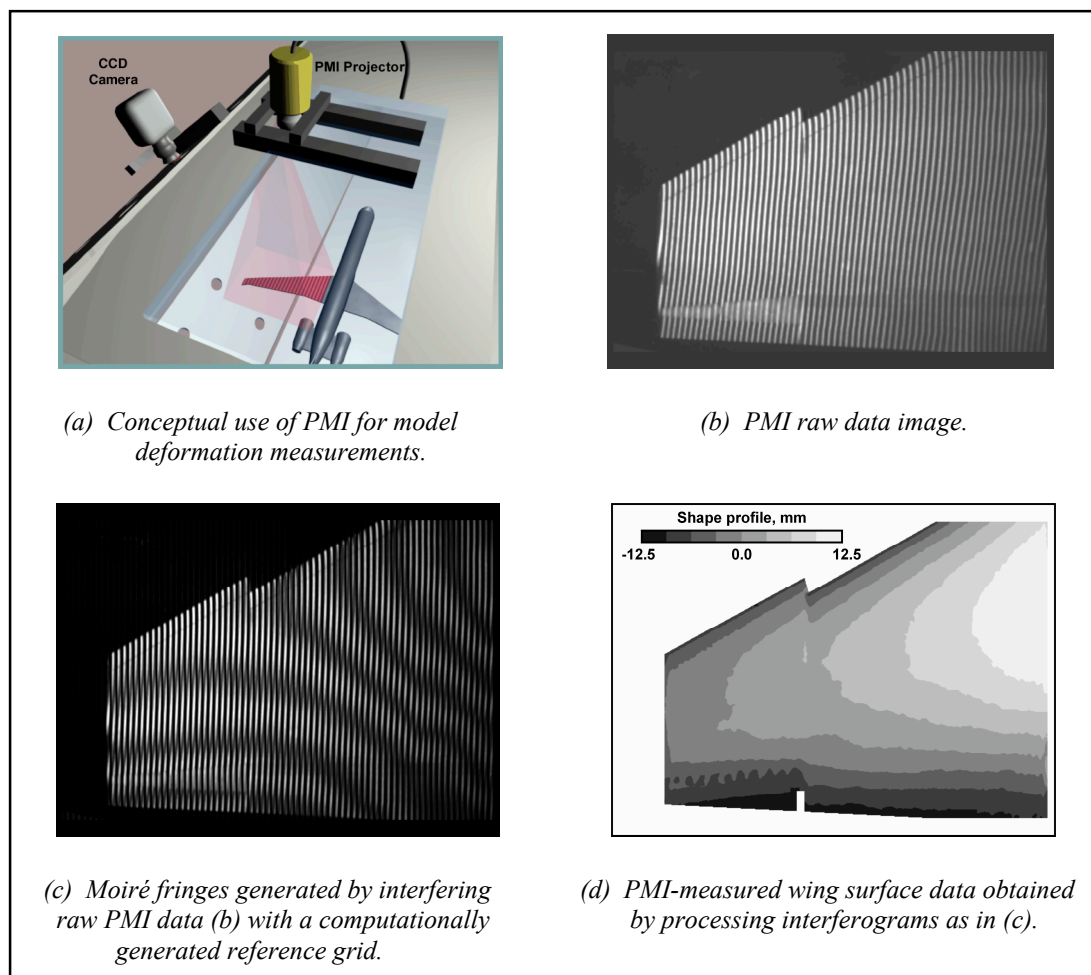


Figure 22. Illustration of the PMI technique.

through a flow expansion slot. A fiber-optically coupled laser diode operating at 790 nm wavelength was used as the projector illumination source. The PMI system video camera was installed in one of the test section light ports directly across from the projector head (Figure 24) and positioned to view the underside of the Smart Wing. The camera contained a standard CCD imager and output RS-170 compatible analog video, which was digitized at 768 x 480 (width x height) pixel resolution using a PC-based video frame grabber. The camera lens was outfitted with a filter whose acceptance band was matched to the projector illumination wavelength. Use of the filter allowed the projected grid line contrast to be preserved in the presence of ambient tunnel lighting by only passing the 790 nm laser light to the CCD imager. A raw PMI data image showing the projected grid pattern is shown in Figure 25(a). The image spatial resolution was 1.76 mm per pixel.

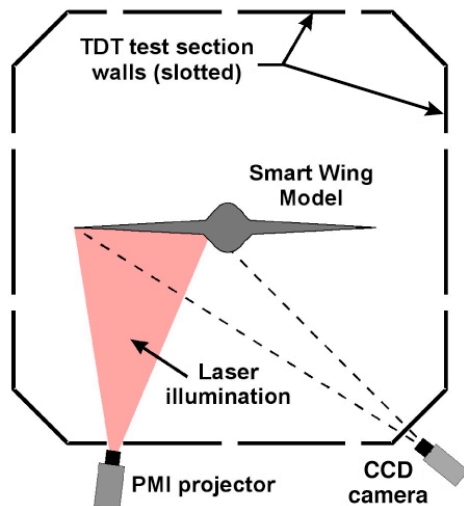


Figure 23. View looking downstream of the TDT test section illustrating the PMI system hardware configuration.

## Results

The primary objective of the PMI system for the final Smart Wing test was to obtain spatially continuous measurements of the entire Smart Wing trailing-edge control surface to (a) validate the trailing-edge deflection angles obtained using the on-board potentiometers and (b) monitor for any unexpected wing / control surface deformation occurring during the course of the test. Such unexpected deformation includes potentially significant changes in the control surface geometry caused by variations in aerodynamic loading as a function of model angle-of-attack (AoA). PMI data were acquired and processed for a majority of



Figure 24. CCD camera installation in TDT light port.

the overall test matrix that involved deflections of the *smart* control surface. Figures 25(b)-(d) show example processed PMI data of the *smart* control surface deflected to  $+7.5^\circ$  uniform,  $\pm 7.5^\circ$  linear variation, and  $+7.5^\circ$  bathtub shapes, respectively. These data were acquired at Mach = 0.8,  $q = 150$  psf, and AoA =  $-0.4^\circ$ . The processed data represent the average change in wing shape compared to a reference image with a non-deflected trailing-edge control surface obtained at the same test conditions.

Processed data images such as those shown in Figures 25(b)-(d) were further analyzed to compute the PMI-measured trailing-edge deflection angles for comparison with those measured using the on-board potentiometers. The procedure used for computing the trailing-edge deflection angles is shown in Figure 26. First, chordwise lines (perpendicular to the leading edge) of deformation data were extracted from the processed PMI data images. Chord lines were extracted from 5- to 95-percent span in 5-percent increments. Regressions were then performed on the linear portions of the control surface deflection profiles at the midspan of each segment to project the trailing-edge tip deflections to 100-percent chord. The trailing-edge deflection angles for each segment were then computed via a 2-point arctangent computation using these computed tip deflection locations and the corresponding locations of the virtual *hingeline*, commensurate with the potentiometers. Offset corrections due to control surface thickness were not required since the PMI system produced differential rather than absolute measurements. Figures 27 – 29 show the comparison between the PMI-measured trailing-edge deflection angle and the on-board potentiometer measurements for the data and test conditions shown in Figures 25(b)-(d), respectively. Error bars have been omitted here for clarity, but during the test, the PMI measurements were

typically found to be within  $\pm 0.17^\circ$  random error ( $\pm 1\sigma$ ) of the potentiometer readings for repeated wind-on measurements. Considering the short chord length ( $\sim 150$  mm) over which the trailing-edge deflection angle was measured, the  $\pm 0.17^\circ$  uncertainty margin equates to a  $\pm 0.44$  mm tip deflection random uncertainty, which is quite small for a PMI system of this magnitude. The PMI and potentiometer data shown in Figures 27 – 29 are in reasonably good quantitative agreement and provide a consistent

representation of the control surface deflection. The root-mean-square (rms) differences of the best fit profiles for the PMI and potentiometer data shown in Figures 27 - 29 were  $0.14^\circ$ ,  $0.69^\circ$ , and  $1.65^\circ$  respectively. The increased disagreement between the PMI and potentiometer measurements for the  $+7.5^\circ$  bathtub deflection case (Figures 25(d) and 29) may be the result of large spanwise gradients in the trailing-edge deflection.

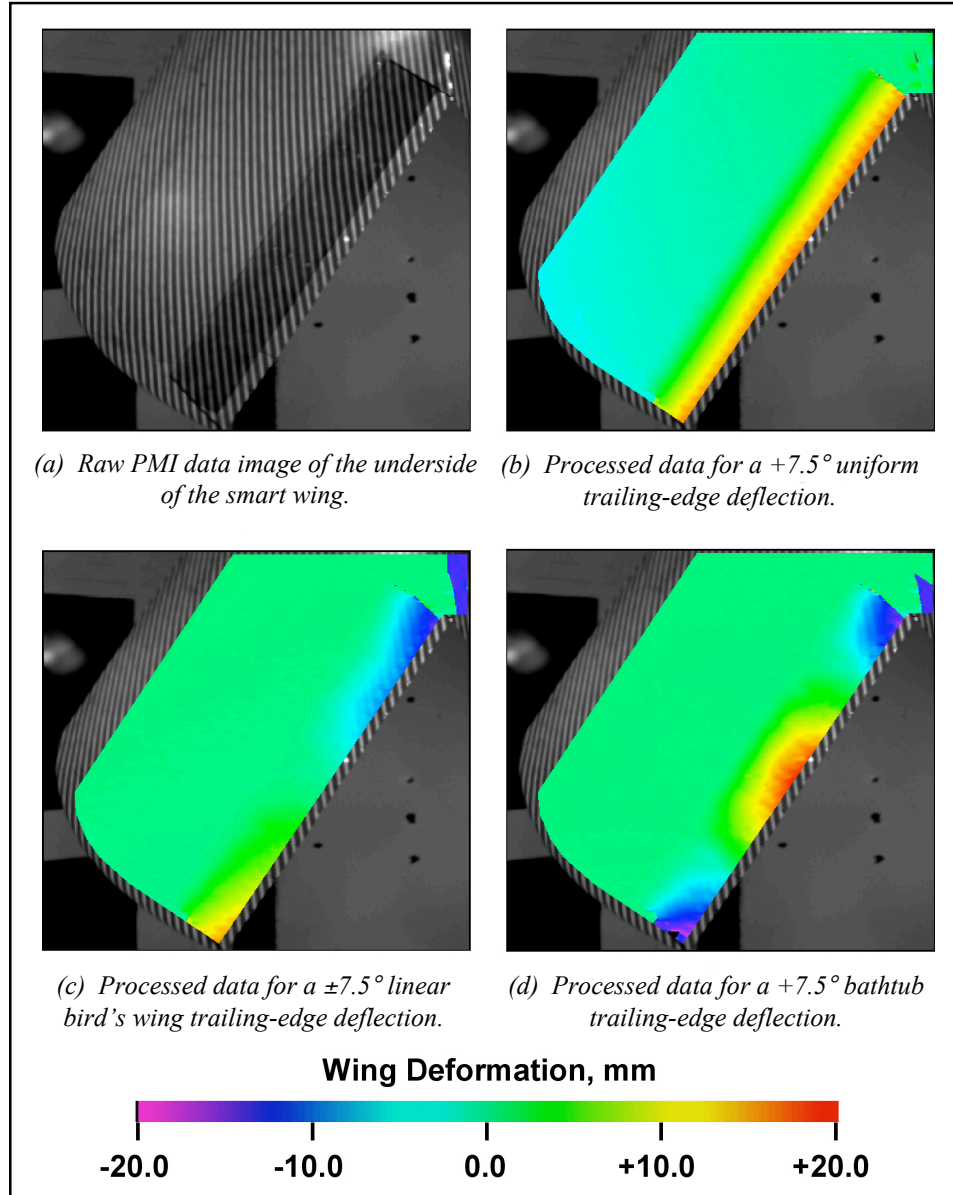


Figure 25. Sample raw and processed PMI data images acquired at  $Mach = 0.8$ ,  $q = 150$  psf, and  $AoA = -0.4^\circ$ .

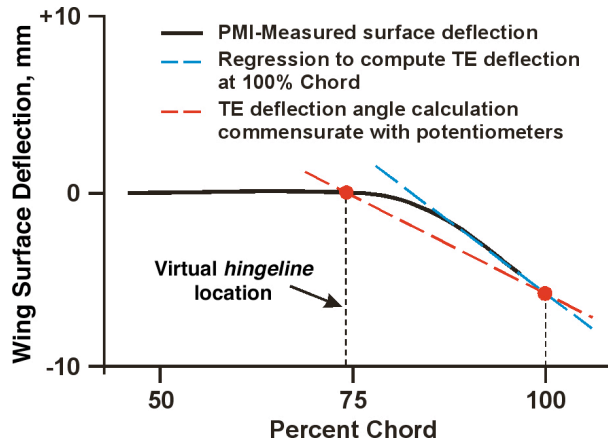


Figure 26. Procedure for computing trailing-edge deflection angle using PMI measurements.

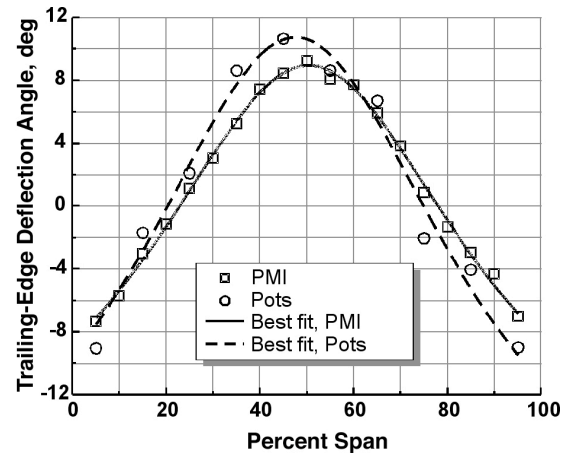


Figure 29. Comparison of PMI and potentiometer measurements for the  $+7.5^\circ$  bathtub case.

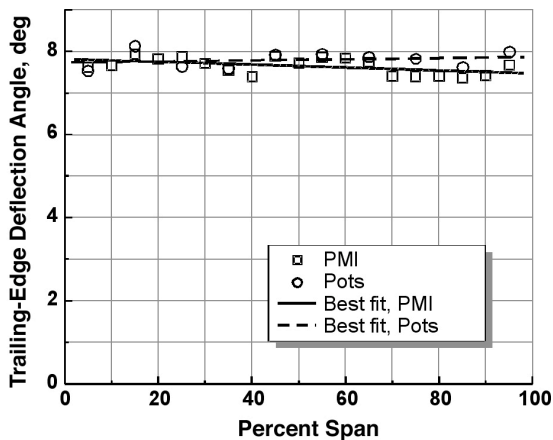


Figure 27. Comparison of PMI and potentiometer measurements for the  $+7.5^\circ$  uniform deflection case.

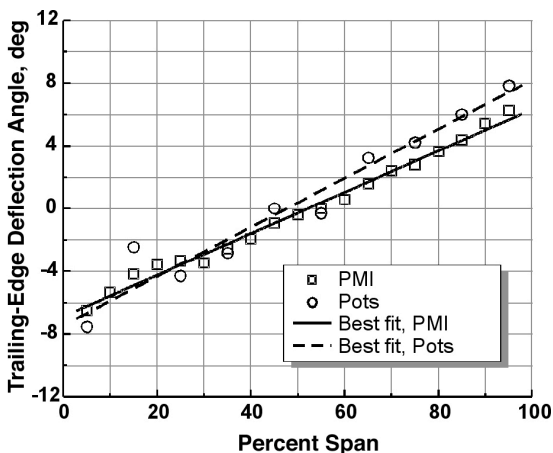


Figure 28. Comparison of PMI and potentiometer measurements for the  $\pm 7.5^\circ$  linear deflection case.

Figures 30 – 32 show the PMI-measured trailing-edge deflection angle as a function of model AoA. The data shown in Figures 31 – 32 show no statistically significant changes in control surface shape as a function of AoA, being consistent to within  $\pm 0.23^\circ$  for both cases. The potentiometer measurements for the same conditions were consistent to within  $\pm 0.18^\circ$ . The data shown in Figure 30, however, does show an increase in the PMI-measured deflection angle on the outboard section of the trailing edge for  $+5.6^\circ$  AoA. This additional deformation was not indicated by the potentiometers. Considering the consistency of the PMI measurements in Figures 31 – 32 throughout the AoA range, it is possible the additional deformation experienced for the  $+7.5^\circ$  uniform deflection case at  $+5.6^\circ$  AoA is real. The additional deformation may be attributable to spanwise wing twist that can be detected by the PMI system, but not with the potentiometers. The on-board potentiometers are "Lagrangian" devices that ride along with the wing, and they are insensitive to changes in wing geometry except for those occurring between the sensor mounting points. In contrast, the PMI system is an "Eularian" device that observes the wing deformation from a fixed reference frame. Therefore the trailing-edge deflection angles measured using the PMI system will be the combined angular deflection, including wing twist, compared to the reference condition, potentially accounting for the increased outboard deformation in Figure 30 at  $+5.6^\circ$  AoA.

In general, the PMI data obtained during the second Smart Wing Phase 2 entry served well to validate the use of the *smart* control surface deflection angles measured with the on-board potentiometers. A review of the full PMI data set also indicated the *smart* wing did not experience any significant unexpected deformations during the course of testing.



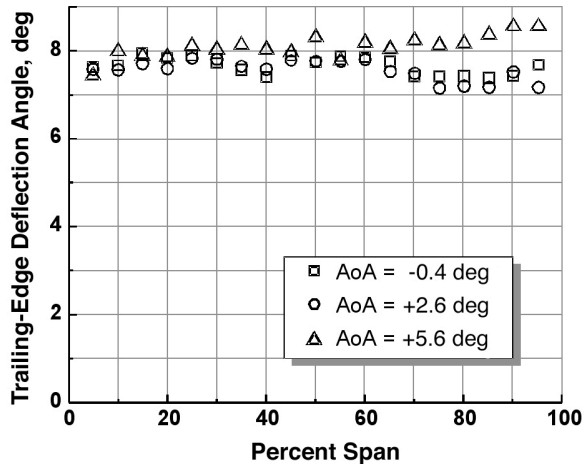


Figure 30. PMI-measured trailing-edge deflection angle as a function of model AoA,  $+7.5^\circ$  uniform.

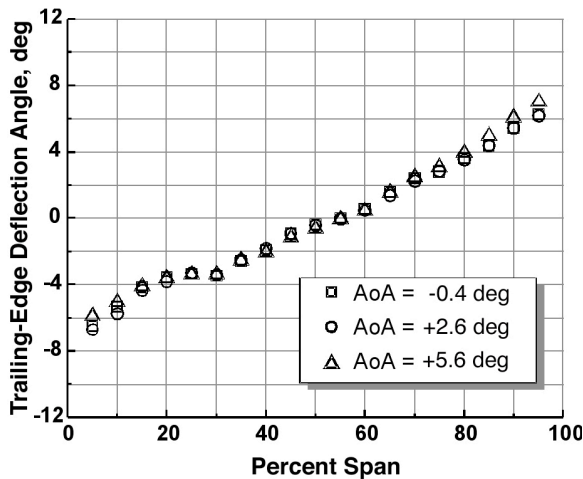


Figure 31. PMI-measured trailing-edge deflection angle as a function of model AoA,  $\pm 7.5^\circ$  linear.

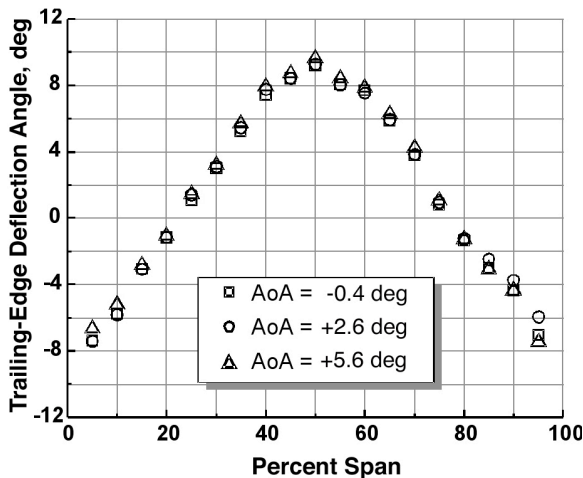


Figure 32. PMI-measured trailing-edge deflection angle as a function of model AoA,  $+7.5^\circ$  bathtub.

## COMPUTATIONAL FLUID DYNAMICS (CFD) SIMULATION

The NASA Langley unstructured computational fluid dynamics (CFD) code “USM3D”<sup>15</sup> was used for Navier-Stokes analysis in the Smart Wing Phase 2 study. Within the tetrahedral cell-centered, finite volume flow solver for this code, inviscid flux quantities are computed across each cell face using Roe’s flux-difference splitting scheme<sup>16</sup>. A novel reconstruction process is used for spatial discretization, based on an analytical formulation for computing gradients within tetrahedral cells, and solutions are advanced to a steady state condition using an implicit backward-Euler time-stepping scheme.

Within USM3D, turbulence closure is given by the Spalart-Allmaras one-equation model<sup>17</sup>. This model solves a single local transport equation for the turbulent viscosity. The turbulence model can be integrated down to the wall, or it can be coupled with a turbulent boundary layer wall function to reduce the number of cells in the sublayer region of the boundary layer. The latter approach was used here.

### Computational Model

The VGRID/GridTool software system<sup>18,19</sup> was used to generate the unstructured grids for this study. VGRID uses an advancing-front method for generating Euler tetrahedral grids and an advancing-layer method for thin-layer tetrahedral viscous grids required for Navier-Stokes analysis. In defining the computational domain, boundaries are represented by bi-linear surface patches that are constructed in GridTool based on CAD geometries. Grid characteristics like cell spacing and stretching are specified in GridTool by the placement of cell “sources”.

A surface mesh is generated in VGRID by triangulating each surface patch with a two-dimensional (2D) version of the advancing-front method. Triangulated surface patches then form the initial “front” for the generation of three-dimensional (3D) tetrahedral volume cells by the advancing-layer and advancing-front methods. Smooth variation of grid spacing is achieved by solving a Poisson equation on a cartesian background grid, using GridTool-defined cell sources as inputs.

A baseline configuration and seven *smart* trailing-edge control surface configurations were analyzed for incorporation in the Smart Wing Phase 2 study. All cases utilized a semi-span grid (suitable for longitudinal control analysis at zero sideslip). The baseline configuration’s semi-span grid with symmetry plane is shown in Figure 33. In all cases, the computational

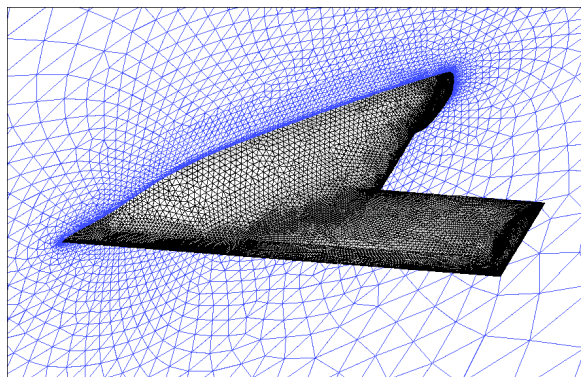


Figure 33. Semi-span grid, baseline configuration.

domain extended roughly 10-14 mean aerodynamic chord lengths from the aircraft CG in all directions. Grid sizes were on the order of 1.5 million tetrahedral cells for simpler cases, ranging up to about 2.5 million cells for complex cases.

One of the primary differences between the NGC UCAV concept configuration and the wind-tunnel model was that the model inlet was faired over. This inlet fairing was duplicated in the CFD model. Because of wind-tunnel sting mounting modifications and other geometric features in the CFD model's CAD definition, the fuselage base region differed between the CFD and wind-tunnel models. Thus, axial force and drag comparisons will not be made here. The CFD-defined control surface shapes and wind-tunnel shapes also differed somewhat because of the inability to accurately predict, pre-test, those shapes. All other features of the wind-tunnel model and CFD model were consistent.

### **Boundary Conditions**

Outer boundaries of the computational domain were treated as characteristic inflow/outflow surfaces with freestream conditions specified by Mach number, Reynolds Number, flow angle, and static temperature. A reflection boundary condition was used at the symmetry plane, and aircraft surfaces were treated as no-slip viscous boundaries. Flow conditions of Mach = 0.6 and  $Re_{Chord} = 3.25 \times 10^6$  were chosen at angles-of-attack (AoAs) of 2°, 3°, 8°, and 10°. The corresponding Reynolds number achieved during the wind-tunnel test was on the order of  $Re_{Chord} = 3.6 \times 10^6$ . In the present paper, CFD results at AoA = 3° will be presented.

### **Solution Procedure**

All solutions presented in this paper were obtained by running USM3D on the "Von Neumann" Cray C-90 and "Bright" Cray SV-1 at NASA Ames, using 10-16

processors in multi-task mode. Typical cases needed 1200-2000 cycles for full convergence and used about 300-500 megawords of memory. During the computation, global CFL number ranged from 5 to approximately 100. Convergence was judged by tracking solution residual until it dropped several orders of magnitude and leveled out. Integrated aerodynamic performance coefficients were used to verify final convergence.

### **Results**

CFD results from two configurations will be discussed and compared to wind-tunnel results in this paper: the baseline configuration (control surface undeflected) and the NGC-defined 10° bathtub shape. The two configurations are shown in Figure 34.

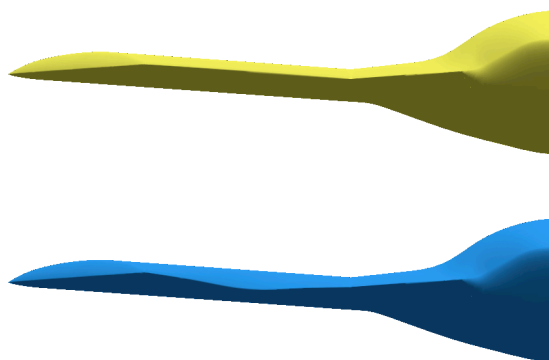


Figure 34. Baseline (top) and 10° bathtub shape (bottom) configurations, as viewed from aft.

A comparison of the trailing-edge control surface geometry between wind-tunnel model and CFD is shown in Figures 35 and 36, quantified in terms of the control-surface deflection angle. The experimental values used were measured by the onboard rotary potentiometers. As shown, there are minor differences in the baseline configuration and larger differences in the 10° bathtub configuration. Overall, however, the actual wind-tunnel model geometries are fairly close to the CAD geometries used in the CFD grids.

Contours of pressure coefficient ( $C_p$ ) on the upper surfaces of the baseline and 10° bathtub configurations are shown in Figures 37 and 38, respectively, at Mach = 0.6,  $Re_{Chord} = 3.25 \times 10^6$ , and AoA = 3°. Results are typical for a highly swept (55°) wing-body at transonic conditions. The 10° bathtub configuration is seen to have lower pressures on the wing upper surface, due to the *smart* control surface deflection.

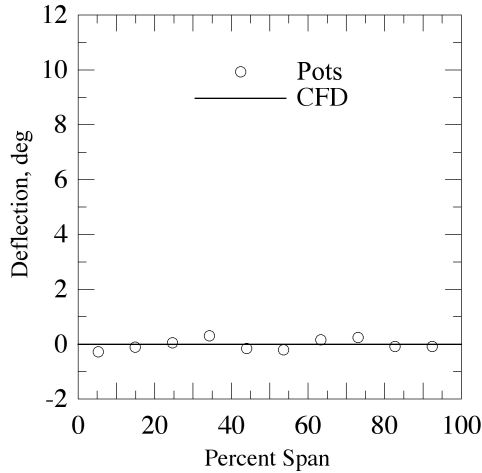


Figure 35. Comparison of wind tunnel (Pots) and CFD trailing-edge deflection, baseline configuration.

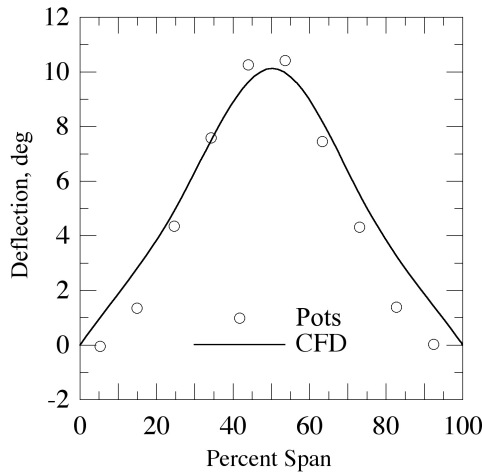


Figure 36. Comparison of wind tunnel (Pots) and CFD trailing-edge deflection, 10° bathtub configuration.

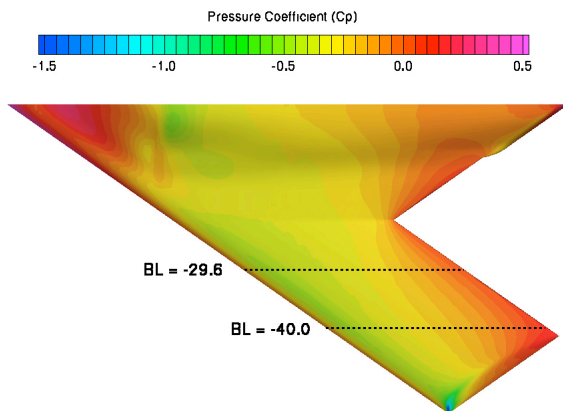


Figure 37. Upper surface pressure coefficient, baseline configuration,  $Mach = 0.6$ ,  $Re_{Chord} = 3.25 \times 10^6$ , and  $AoA = 3^\circ$ .

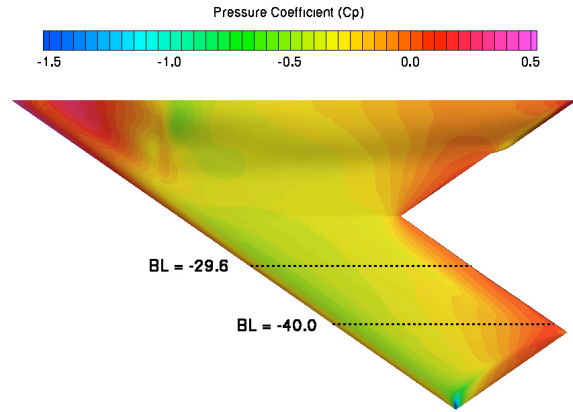


Figure 38. Upper surface pressure coefficient, 10° bathtub configuration,  $Mach = 0.6$ ,  $Re_{Chord} = 3.25 \times 10^6$ , and  $AoA = 3^\circ$ .

Streamwise distributions of pressure coefficient at mid-span ( $BL = -29.6$  inches) and outboard ( $BL = -40.0$  inches) locations are shown in Figures 39 – 42 for the CFD simulation at  $AoA = 3^\circ$  and wind-tunnel data taken at  $AoA = 2.6^\circ$ . The overall agreement between wind tunnel and CFD is reasonable and consistent with the variations that existed between the CFD geometry and the wind-tunnel model and the minor differences in  $AoA$  and Reynolds number. The effect of the trailing-edge control surface deflection is apparent on the pressure distribution in Figures 41 and 42; upper surface pressure is decreased, and lower surface pressure is increased in the 10° bathtub configuration when compared to the baseline.

Lift and pitching moment coefficients for the baseline and 10° bathtub configurations are shown in Figures 43 – 46, where the CFD prediction at  $AoA = 3^\circ$  is compared to wind-tunnel data taken at  $AoAs$  from  $0.6^\circ$  to  $7.6^\circ$ . At  $AoA = 3^\circ$ , CFD-predicted lift and pitching moment coefficient are within 3–10% of the wind-tunnel data, which is inline with differences seen in the surface pressure distributions.

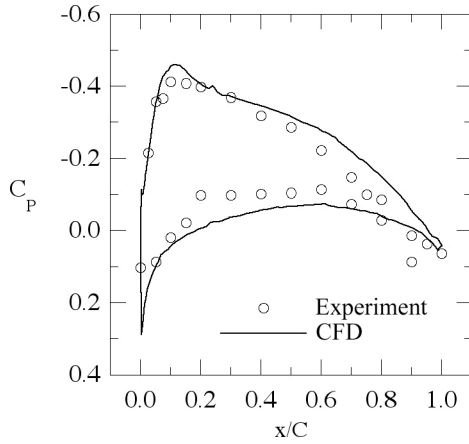


Figure 39. Local streamwise  $C_p$  distribution at  $BL = -29.6$  inches, baseline configuration,  $Mach = 0.6$ ,  $Re_{Chord} = 3.25 \times 10^6$ ,  $AoA = 3^\circ$  (CFD),  $2.6^\circ$  (Exp.).

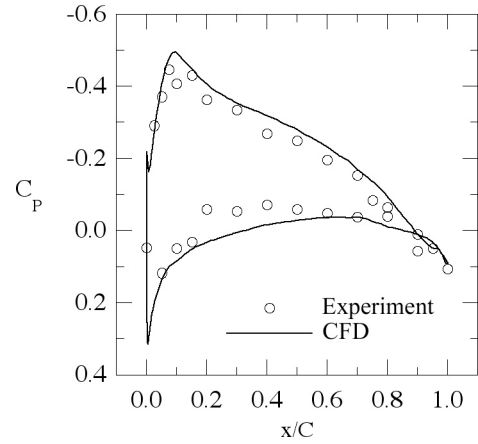


Figure 42. Local streamwise  $C_p$  distribution at  $BL = -40.0$  inches,  $10^\circ$  bathtub configuration,  $Mach = 0.6$ ,  $Re_{Chord} = 3.25 \times 10^6$ ,  $AoA = 3^\circ$  (CFD),  $2.6^\circ$  (Exp.).

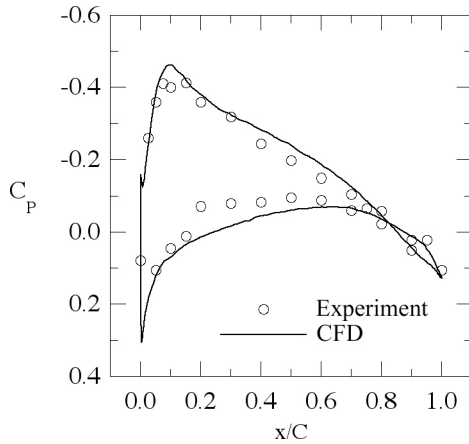


Figure 40. Local streamwise  $C_p$  distribution at  $BL = -40.0$  inches, baseline configuration,  $Mach = 0.6$ ,  $Re_{Chord} = 3.25 \times 10^6$ ,  $AoA = 3^\circ$  (CFD),  $2.6^\circ$  (Exp.).

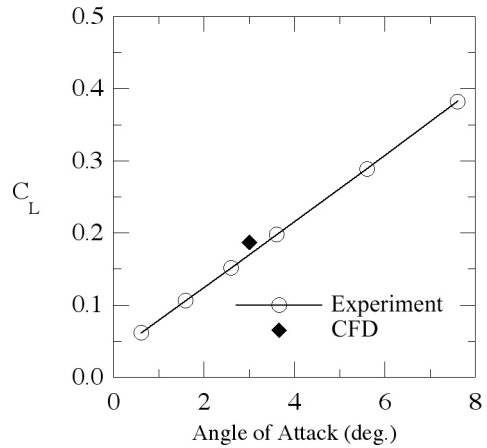


Figure 43. Comparison of lift coefficient between wind-tunnel data and CFD prediction, baseline configuration,  $Mach = 0.6$ ,  $Re_{Chord} = 3.25 \times 10^6$ .

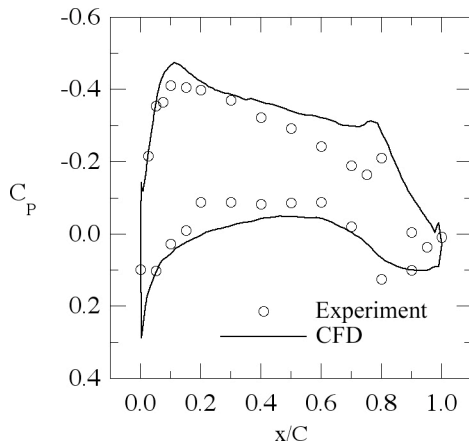


Figure 41. Local streamwise  $C_p$  distribution at  $BL = -29.6$  inches,  $10^\circ$  bathtub configuration,  $Mach = 0.6$ ,  $Re_{Chord} = 3.25 \times 10^6$ ,  $AoA = 3^\circ$  (CFD),  $2.6^\circ$  (Exp.).

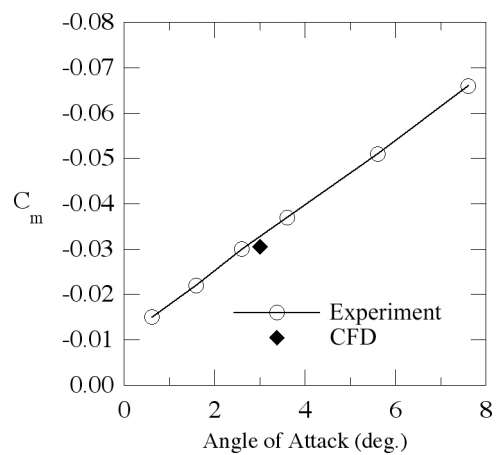


Figure 44. Comparison of pitching moment coefficient between wind-tunnel data and CFD prediction, baseline configuration,  $Mach = 0.6$ ,  $Re_{Chord} = 3.25 \times 10^6$ .

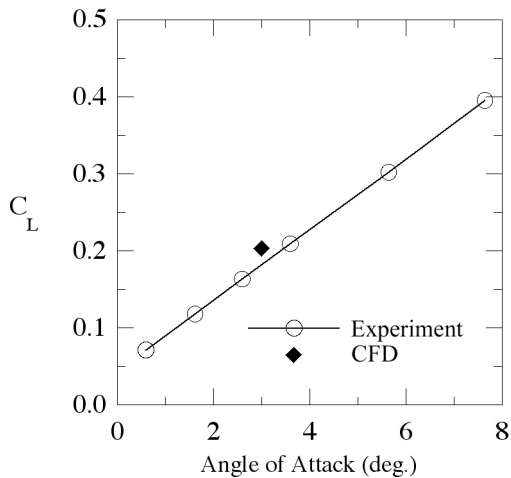


Figure 45. Comparison of lift coefficient between wind-tunnel data and CFD prediction, 10° bathtub configuration,  $Mach = 0.6$ ,  $Re_{Chord} = 3.25 \times 10^6$ .

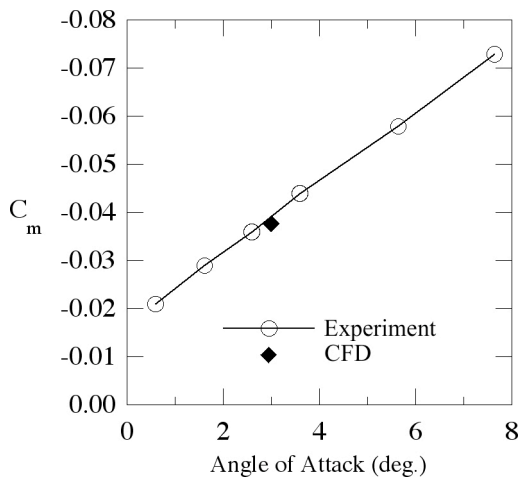


Figure 46. Comparison of pitching moment coefficient between wind-tunnel data and CFD prediction, 10° bathtub configuration,  $Mach = 0.6$ ,  $Re_{Chord} = 3.25 \times 10^6$ .

## CONCLUSION

The Smart Wing program was a highly successful collaboration between DARPA, AFRL, NASA, and the Northrop Grumman Corporation (NGC). NASA LaRC's roles were to provide technical guidance, wind-tunnel testing time and support in the Langley Transonic Dynamics Tunnel (TDT), and CFD analyses. For the fourth and final TDT entry in April/May 2001, a model based on the NGC UCAV concept was tested at Mach numbers up to 0.8 and dynamic pressures up to 150 psf. The model was a 30% geometric scale, full-span, sting-mounted model with hingeless, smoothly-contoured *smart* control surfaces on the starboard wing and conventional hinged control surfaces on the port

wing. During the entry, deflections of the *smart* control surfaces were measured both internally by rotary potentiometers and externally by two independent LaRC systems: VMD and PMI. Overall, the VMD and PMI data obtained served well to validate the deflection angles measured by the potentiometers. For most of the test, typical differences between the potentiometer and VMD measured angles ranged from 6-13%. PMI results for three sample NGC-defined shapes showed measurements to be within 0.17° random error of the potentiometers, with rms differences ranging from 0.14° to 1.65°. One possible reason for these discrepancies was the ability of the two external systems to measure aerodynamic and aeroelastic effects, such as flow-induced wing twist. The internal potentiometers were incapable of detecting such changes in the chordwise and spanwise deflection profiles. A second source of error was the calibration of the external systems at a single angle-of-attack. NASA CFD analysis performed for the final wind-tunnel test did not precisely match wind-tunnel results when the control surface was deflected because the predicted CAD control surface geometries differed from the actual shapes tested. However, results matched fairly well for the undeflected baseline case. All three NASA efforts discussed herein provided significant insight into the behavior of the high-actuation rate, hingeless, smoothly-contoured Smart Wing control surfaces.

## ACKNOWLEDGEMENTS

The authors would like to express their sincere appreciation to the other members of the NASA LaRC team responsible for making the final Smart Wing wind-tunnel test so successful. These valued team members include: Harriett Dismond and Ken Cate (VMD team), Hector Soto and Bruce South (PMI team), Carol Wieseman, James Florance, Chuck McClish, and Jerry Garcia (TDT test team), Tom Finley and Brad Crawford (Sting Whip team), John Hoppe and Scott Sealey (Optotrak® team), and John Lamar (technical guidance). The authors would also like to acknowledge the Northrop Grumman test team for their support and cooperation during all phases of the Smart Wing program.

## REFERENCES

1. Smart Materials and Structures – Smart Wing Phase 1, Volumes I, II, III, and IV, Contract Final Report, AFRL-ML-WP-TR-1999-4162, Contract Number F33615-95-C-3202, December 1998.



2. Kudva, Jayanth N.; Martin, Christopher A.; Scherer, Lewis B.; Jardine, A. Peter; McGowan, Anna-Maria Rivas; Lake, Renee C.; Sendekyj, George P.; Sanders, Brian P., "Overview of the DARPA/AFRL/NASA Smart Wing program", SPIE Conference on Smart Structures and Materials, Industrial and Commercial Applications of Smart Structures Technologies, Paper #3674-26, pp. 230-236, July 1999.
3. Kudva, J. N.; Sanders, B.; Pinkerton-Florance, J.; Garcia, E., "Overview of the DARPA/AFRL/NASA Smart Wing Phase 2 Program", SPIE Conference on Smart Structures and Materials, Industrial and Commercial Applications of Smart Structures Technologies, Paper #4332-48, pp 383-389, June 2001.
4. Martin, C. A.; et al, "Design, Fabrication and Testing of the Scaled Wind Tunnel Model for the Smart Wing Phase 2 Program", SPIE's 9th Annual Symposium on Smart Structures and Materials, Paper #4698-05, pp 44-52, July 2002.
5. Bartley-Cho, Jonathan D.; Wang, D. P.; West, Mark N., "Development, Control, and Test Results of High Rate, Hingeless Trailing Edge Control Surface for the Smart Wing Phase 2 Wind Tunnel Model", SPIE's 9th Annual Symposium on Smart Structures and Materials, Paper #4698-06, pp 53-63, July 2002.
6. Kudva, J. N.; Sanders, B.; Pinkerton-Florance, J.; Garcia, E., "DARPA/AFRL/NASA Smart Wing Program: Final Overview", SPIE's 9th Annual Symposium on Smart Structures and Materials, Paper #4698-04, pp 37-43, July 2002.
7. Scherer, L. B.; et al, "DARPA/AFRL Smart Wing Phase 2 Wind Tunnel Test Results", SPIE's 9th Annual Symposium on Smart Structures and Materials, Volume 4698, Paper # 4698-07, pp 64-75, July 2002.
8. Smart Materials and Structures – Smart Wing Phase 2, Contract Final Report, Contract Number F33615-97-C-3213, Expected Publication July 2003.
9. *The NASA Langley Transonic Dynamics Tunnel*, LWP-799, September 1969.
10. Burner, A. W.; Liu, Tianshu, "Videogrammetric Model Deformation Measurement Technique", Journal of Aircraft, Vol. 38, No. 4, pp. 745-754, July-August, 2001.
11. Graves, Sharon S.; Burner, Alpheus W., "Development of an Intelligent Videogrammetric Wind Tunnel Measurement System", SPIE's 46th Annual Meeting--The International Symposium on Optical Science and Technology, Vol. 4448, pp. 120-131, July 29-August 3, 2001.
12. Fleming, G. A.; Burner, A. W., "Deformation Measurements of Smart Aerodynamic Surfaces", SPIE International Symposium on Optical Science, Engineering, and Instrumentation, Denver, CO, July 18-23, 1999.
13. Martin, C. A.; Scherer, L. B.; West, M. N.; Florance, J.; Wieseman, C.; Burner, A. W.; Fleming, G. A., "DARPA/ARFL/NASA Smart Wing second wind tunnel test results", SPIE's 6th Annual International Symposium on Smart Structures and Materials, Industrial and Commercial Applications of Smart Structures Technologies, Paper # 3674-28, March 1-5, 1999.
14. Fleming, G. A.; Soto, H. L.; South, B. W., "Projection Moiré Interferometry for Rotorcraft Applications: Deformation Measurements of Active Twist Rotor Blades", American Helicopter Society 58th Annual Forum, Montreal, Canada, June 10-13, 2002.
15. Frink, N., "Tetrahedral Unstructured Navier-Stokes Method for Turbulent Flows", AIAA Journal, Vol. 36, No. 11, pp 1975-1982, November 1998.
16. Roe, P.L., "Approximate Riemann solvers, parameter vectors, and difference schemes", Journal of Computational Physics, Volume 43, pp 357-372, 1981.
17. Spalart, P.R.; Allmaras, S.R., "A One-Equation Turbulence Model for Aerodynamic Flows", AIAA 92-0439, January 1992.
18. Pirzadeh, S., "Progress Toward a User-Oriented Unstructured Viscous Grid Generator", AIAA 96-0031, January 1996.
19. Samareh, J., "GridTool: A Surface Modeling and Grid Generation Tool", Proceedings of the Workshop on Surface Modeling, Grid Generation, and Related Issues in CFD Solutions, NASA CP-3291, May 1995.